

CESTsimu: An open-source GUI for spectral and spatial CEST simulation

Huabin Zhang^{1,2}  | Bensheng Qiu²  | Jiadi Xu^{3,4}  | Kannie WY Chan^{3,5}  | Jianpan Huang¹ 

¹Department of Diagnostic Radiology, Li Ka Shing Faculty of Medicine, The University of Hong Kong, Hong Kong, China

²Department of Electronic Engineering and Information Science, University of Science and Technology of China, Hefei, China

³Russell H. Morgan Department of Radiology and Radiological Science, Johns Hopkins University School of Medicine, Baltimore, Maryland, USA

⁴F. M. Kirby Research Center for Functional Brain Imaging, Kennedy Krieger Institute, Baltimore, Maryland, USA

⁵Department of Biomedical Engineering, City University of Hong Kong, Hong Kong, China

Correspondence

Jianpan Huang, Department of Diagnostic Radiology, Li Ka Shing Faculty of Medicine, The University of Hong Kong, 5 Sassoon Road, Pokfulam, Hong Kong, China.

Email: jphuang@hku.hk

Funding information

National Natural Science Foundation of China, Grant/Award Number: 82402225; The University of Hong Kong, Grant/Award Numbers: 109000487, 200000341, 109001694; Li Ka Shing Faculty of Medicine, The University of Hong Kong, Grant/Award Numbers: 204610401, 204610519; Health and Medical Research Fund, Grant/Award Number: 21222621

Abstract

Purpose: The aim of this study was to create a user-friendly CEST simulation tool with a GUI for both spectral (1D Z-spectra) and spatial (2D phantom) CEST experiments, making the CEST simulation easier to perform.

Methods: CESTsimu was developed using MATLAB App Designer. It consists of three modules: Saturation Settings, Exchange Settings, and Phantom Settings. CESTsimu can not only import/export files in the defined format but can also import files generated by other existing simulation platforms (e.g. pulseq-CEST).

Results: The 1D Z-spectrum simulation results demonstrated the effectiveness of CESTsimu in simulating Z-spectra under various saturation (B_0 and B_1) and exchange settings (concentration and exchange rate). The 2D simulation results showed that CESTsimu can generate an arbitrary number of phantoms with different shapes under different noise conditions. Notably, CESTsimu could also simulate B_0 and B_1 inhomogeneity in 2D patterns that mimicked practical conditions. Moreover, the accuracy of CESTsimu was validated by simulating 8 cases in the BMsim challenge.

Conclusion: We developed a user-friendly CESTsimu GUI for intuitively simulating CEST experiments under diverse saturation and exchange settings in 1D and 2D conditions. CESTsimu has the potential to facilitate the broad utilization of CEST MRI among a wide range of users.

KEY WORDS

B_0 and B_1 inhomogeneity, 1D Z-spectra, 2D phantom, Bloch-McConnell equation, CEST simulation, graphical user interface

1 | INTRODUCTION

Chemical exchange saturation transfer (CEST) imaging is a powerful molecular MRI technique that leverages the exchange of protons between water and various compounds to image low-concentration molecules. It can be used to detect multiple endogenous exchangeable protons in molecules, such as amide protons in proteins and peptides (amide proton transfer, APT),^{1–3} amine protons in glutamate,^{4–6} aliphatic/olefinic or aromatic protons in mobile macromolecules such as lipids (nuclear Overhauser effect, NOE),^{7–9} hydroxyl protons in sugars,^{10–12} and guanidinium protons (Guan) in creatine (Cr), phosphocreatine (PCr), and mobile proteins.^{13–16} Using specific acquisition settings and data analysis methods,^{17,18} magnetization transfer contrast (MTC) caused by macromolecules can also be extracted in CEST experiments. By examining the semi-solid macromolecules (MTC), mobile macromolecules (APT and NOE), and metabolites (e.g., glucose and creatine), CEST has shown promise in diagnosing a series of diseases, including brain tumors,^{19,20} neurodegenerative diseases,^{21,22} breast cancer,^{23,24} prostate cancer,²⁵ and liver diseases.²⁶

Bloch equations²⁷ serve as the foundation for modeling the spatiotemporal movement of the macroscopic magnetization of spins in external fields that are static or vary over time. Bloch-McConnell (BM) equations are an extended Bloch model that accounts for chemical exchange between water protons and other exchangeable solute protons.²⁸ The BM equations (BME) are commonly used for sequence optimization,^{29,30} simulation data generation,^{31,32} and post-experiment verification³³ in CEST or magnetization transfer (MT) experiments. BM-based CEST data fitting utilizes the BME to model the dynamics of magnetization exchange between proton pools, which yields quantitative parameters such as exchange rate and concentration.^{34–36} Because of the wide application of BME, the accuracy of BM simulation has drawn much attention over the past years. Despite using the same BME, the BM simulations performed by different groups may display apparent discrepancies, resulting in significant variations in the quantifiable parameters. Recently, the BM simulation (BMsim) challenge has been initiated with the ultimate goal of standardizing BM simulation in CEST studies.³⁷ The standardization of BM simulation is not only crucial for CEST simulation but is also essential for interpreting data from practical CEST experiments. It can help establish more reproducible and interpretable CEST MRI techniques.

Previous research has introduced open-source platforms to aid users in conducting CEST simulation experiments. Graphical user interface (GUI) based platforms like SpinBench,³⁸ JEMRIS,³⁹ and MRILab⁴⁰ offer realistic

MRI simulations with great flexibility, allowing users to define entire MRI experiments via both GUI and code. This capability is especially useful for validating new MRI approaches designed to quantitatively assess tissue composition and microstructure. While JEMRIS and MRI-Lab are general MRI simulation platforms with many functions that may not be necessary for CEST simulation, a more CEST-dedicated simulation package named Pulseq-CEST⁴¹ utilizes the Pulseq⁴² framework to define and perform CEST simulation through human-readable files. The software simplifies the sharing, implementation, testing, optimization, and execution of CEST simulation across various MR sites, thereby improving reproducibility among different research groups in both simulation and practical experiments. Nonetheless, pulseq-CEST lacks a GUI, and users must configure parameter settings in the code, which makes it less intuitive especially for users without programming experience.

In this study, we have developed a user-friendly CEST simulation (CESTsimu) platform with a GUI that enables intuitive spectral (1D Z-spectrum) and spatial (2D phantom) CEST simulations with simple and straightforward parameter settings. Specifically, CESTsimu consists of three modules: “Saturation Settings”, “Exchange Settings” and “Phantom Settings”. We performed four experiments to validate the accuracy and practicality of CESTsimu: (i) 1D simulation to show the effectiveness of CESTsimu in generating Z-spectra under various CEST settings; (ii) 2D simulation to demonstrate the capability of CESTsimu in mimicking CEST imaging of phantom with different spatial patterns; (iii) B_0 and B_1 inhomogeneity experiment to show the feasibility of adding ΔB_0 and ΔB_1 that commonly occur in practical experiments; (iv) Accuracy verification by simulating 8 simulation cases in BMsim challenge.

2 | METHODS

2.1 | BME solver

CESTsimu calculates the CEST signal based on the BME, which incorporates the exchange reactions among spin pools into the Bloch equation. The evolution of the magnetization vectors for a two-pool model can be described using the BME⁴³:

$$\begin{aligned} \frac{d\vec{M}_w}{dt} &= \mathfrak{R}_w(t)\vec{M}_w - R_w(\vec{M}_w - \vec{M}_{0w}) \\ &\quad - k_{ws}\vec{M}_w + k_{sw}\vec{M}_s, \\ \frac{d\vec{M}_s}{dt} &= \mathfrak{R}_s(t)\vec{M}_s - R_s(\vec{M}_s - \vec{M}_{0s}) \\ &\quad - k_{sw}\vec{M}_s + k_{ws}\vec{M}_w, \end{aligned} \quad (1)$$

where vector $\vec{M}_w = (M_{xw}, M_{yw}, M_{zw})$ and vector $\vec{M}_s = (M_{xs}, M_{ys}, M_{zs})$ are the magnetization vectors of water pool w and solute pool s respectively, with the time variable t omitted for simplicity. \vec{M}_{0w} and \vec{M}_{0s} are the thermal equilibrium magnetization vectors proportional to the pool concentration. k_{ws} is the exchange rate from pool w to pool s , and k_{sw} is the exchange rate from pool s to pool w . The relationship between k_{ws} and k_{sw} is given by⁴³: $k_{ws}f_w = k_{sw}f_s$, where f_w and f_s are the relative proton fractions of pool w and pool s respectively. Only the first-order exchange process is considered since the higher-order exchange reactions can be treated as pseudo-first-order rate constants.⁴⁴ $\mathfrak{R}_i(t)$ and R_i ($i = w, s$) are the rotation matrix and the relaxation matrix respectively, which are formulated in the rotating frame at the radiofrequency (RF) carrier frequency ω_{RF} and written as⁴⁵:

$$\begin{aligned}\mathfrak{R}_i(t) &= \begin{bmatrix} 0 & -\Delta\omega_i & -\gamma B_{1y}(t) \\ \Delta\omega_i & 0 & \gamma B_{1x}(t) \\ \gamma B_{1y}(t) & -\gamma B_{1x}(t) & 0 \end{bmatrix}, \\ R_i &= \begin{bmatrix} 1/T_{2,i} & 0 & 0 \\ 0 & 1/T_{2,i} & 0 \\ 0 & 0 & 1/T_{1,i} \end{bmatrix},\end{aligned}\quad (2)$$

where $\Delta\omega_i = \omega_{RF} - \omega_i$ is the RF frequency offset relative to the Larmor frequency ω_i of pool i (for water pool with ^1H protons, $\omega_w/B_0 = \gamma = 2\pi \cdot 42.576 \text{ rad} \cdot \mu\text{T}^{-1} \cdot \text{s}^{-1}$, B_0 is the static field), $B_{1x/y}$ is the amplitude component of the RF waveform on the X/Y axis, $T_{1,i}$ and $T_{2,i}$ are the longitudinal relaxation time and the transverse relaxation time of pool i . The CESTsimu further defines two variables (in units of ppm): frequency offset $\Delta\omega = (\omega_{RF} - \gamma B_0)/(\gamma B_0)$ and pool offset $\delta\omega_i = (\omega_i - \gamma B_0)/(\gamma B_0)$.

The two-site BME (1) can be easily extended to multi-pool scenarios by incorporating linear exchange terms. A three-pool BME with two solute pools s_1 and s_2 can be expressed as a non-homogeneous first-order ordinary differential equation (ODE):

$$\begin{aligned}\frac{d}{dt}\vec{M} &= A\vec{M} + \vec{C}, \\ \vec{M} &= \begin{bmatrix} \vec{M}_w \\ \vec{M}_{s_1} \\ \vec{M}_{s_2} \end{bmatrix}, \quad \vec{C} = \begin{bmatrix} R_w & 0 & 0 \\ 0 & R_{s_1} & 0 \\ 0 & 0 & R_{s_2} \end{bmatrix} \begin{bmatrix} \vec{M}_{0w} \\ \vec{M}_{0s_1} \\ \vec{M}_{0s_2} \end{bmatrix}, \\ A &= \begin{bmatrix} \mathfrak{R}_w(t) - R_w & 0 & 0 \\ 0 & \mathfrak{R}_{s_1}(t) - R_{s_1} & 0 \\ 0 & 0 & \mathfrak{R}_{s_2}(t) - R_{s_2} \end{bmatrix} \\ &+ \begin{bmatrix} -D(k_{w,s_1} + k_{w,s_2}) & D(k_{s_1,w}) & D(k_{s_2,w}) \\ D(k_{w,s_1}) & -D(k_{s_1,w}) & 0 \\ D(k_{w,s_2}) & 0 & -D(k_{s_2,w}) \end{bmatrix},\end{aligned}\quad (3)$$

where the rotation matrix \mathfrak{R}_i and relaxation matrix R_i ($i = w, s_1, s_2$) are defined in (3), $D(\cdot)$ denotes a diagonal matrix operator.

Since MR scanners generate RF waveforms in discrete form, the coefficient matrix A in (3) remains time-invariant within each interval $[t_n, t_{n+1})$. Thus, the temporal evolution of magnetization vectors can be computed interval by interval, with the coefficient matrix at $[t_n, t_{n+1})$ defined as $A_n \triangleq A(t = t_n)$.

The solution to an inhomogeneous ODE combines the general solution of the homogeneous ODE, $\vec{M}_h^n(t)$, and a particular solution of the inhomogeneous ODE, $\vec{M}_p^n(t)$. Here, the superscript n denotes the magnetization vector within $[t_n, t_{n+1})$. The general solution \vec{M}_h^n is derived from the homogeneous first-order ODE, while the steady-state solution \vec{M}_p^n is obtained by setting the first derivative of $\vec{M}^n(t)$ to zero^{46,47}:

$$\begin{aligned}\vec{M}_h^n(t) &= \mathbb{C}e^{A_n t}, \quad t \in [0, t_{n+1} - t_n], \\ \vec{M}_p^n &= -A_n^{-1}\vec{C},\end{aligned}\quad (4)$$

where constant \mathbb{C} is determined by the initial condition $\vec{M}^n(t = 0) = \vec{M}_f^{n-1}$, and \vec{M}_f^{n-1} represents the final magnetization vector in the time interval $[t_{n-1}, t_n]$. By substituting this initial condition, the recurrence relationship for the total magnetization vector at adjacent time points can be derived:

$$\begin{aligned}\vec{M}^n(t) &= \vec{M}_h^n(t) + \vec{M}_p^n(t) \\ &= \left(\vec{M}_f^{n-1} + A_n^{-1}\vec{C} \right) e^{A_n t} - A_n^{-1}\vec{C}, \\ t &\in [0, t_{n+1} - t_n].\end{aligned}\quad (5)$$

If only the final magnetization vectors of each time interval are considered, and the time step size is defined as $\tau_n = t_{n+1} - t_n$, then the iterative expression of the magnetization vector \vec{M}_f^n at adjacent time point can be written as:

$$\vec{M}_f^n = \left(\vec{M}_f^{n-1} + A_n^{-1}\vec{C} \right) e^{A_n \tau_n} - A_n^{-1}\vec{C}. \quad (6)$$

By using the MATLAB built-in function “expm” and setting constant vector \vec{C} determined by pool concentration and relaxation parameters, CESTsimu can simulate the evolution of the magnetization vector based on the BME under various saturation and exchange settings.

2.2 | CESTsimu layout

In this study, CESTsimu GUI was developed using MATLAB App Designer. No additional MATLAB toolbox is

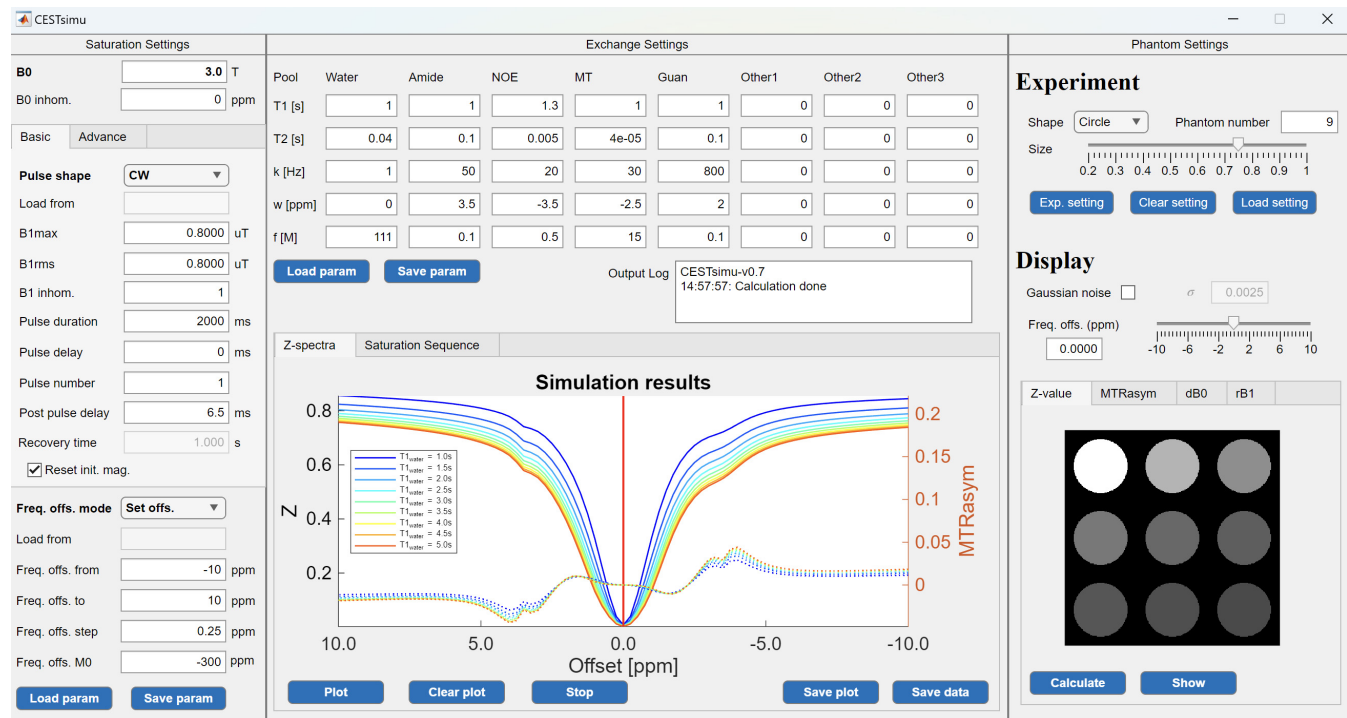


FIGURE 1 Layout of CESTsimu GUI, which consists of three modules: “Saturation Settings”, “Exchange Settings”, and “Phantom Settings”.

required when installing the CESTsimu App. It allows users to easily set or adjust CEST parameters under the “Saturation Settings”, “Exchange Settings”, and “Phantom Settings” modules (Figure 1). Other than the manual setting, users can expedite the configuration of simulation parameters by importing two pre-stored files, defining saturation module and exchange pool respectively, from CES-Tsimu (.SATPARA and .EXCPARA) or Pulseq-CEST (.SEQ and .YAML).⁴¹

2.2.1 | Saturation Settings

In the “Saturation Settings” module, users can define the main magnetic field strength (B_0), saturation pulse (B_1), and frequency offset list through input boxes in the GUI. The B_0 is characterized by its amplitude in Tesla (T) and scalar B_0 inhomogeneity in ppm. The saturation pulse parameters include pulse shape, B_1 maximum amplitude ($B_{1\text{max}}$), B_1 root mean square amplitude ($B_{1\text{rms}}$),⁴⁸ scalar relative B_1 inhomogeneity, pulse duration, interpulse delay, pulse repetition number, post-pulse delay, and pulse phase cycling pattern (in the “Advance” tab). Users can select from pre-defined pulse shapes, such as continuous wave (CW), sinc pulse, Gaussian pulse, and Fermi pulse, or import pulse shapes from formatted text files, including SATPARA-files (CESTsimu files that store saturation settings) and SEQ-files (Pulseq sequence files). The

“Reset init. mag.” checkbox is used to reset the magnetization vector to the steady state before the saturation. When this checkbox is ticked, the “Recovery time” input box will be disable, and the relaxation before the saturation is not considered. In the “Advance” tab shown in Figure 2A, the user can define the number of sampling points per shaped RF pulse, with the default value being 200. The “Comp. accum. phase” checkbox can also be used to compensate the accumulated pulse phase in the pulsed saturation where multiple off-resonant RF chains will cause accumulated phase error due to different rotating coordinate systems.⁴⁹

The CEST frequency offset list can be defined in either “Set offs.” mode or “Load offs.” mode. In “Set offs.” mode, CESTsimu simulates Z-spectra using an equidistant frequency offset array defined through the UI. The start and end frequency offsets are defined by “Freq. offs. from” and “Freq. offs. to”, respectively, with a step size defined by “Freq. offs. step”. In “Load offs.” mode, users can import arbitrary frequency offset lists from formatted text files (SATPARA-files or SEQ-files). M_0 can be defined by “Freq. offs. M0”. It must be defined independently. Notably, all parameters in the “Saturation Settings” module can be loaded from either SATPARA-files or SEQ-files and exported to an integrated SATPARA-files. The “Pulse shape” dropdown menu offers “CW”, “Sinc”, “Gauss”, “Fermi”, and “Other”. The “Freq. offs. mode” dropdown menu includes “Set offs.” and “Load offs.”.

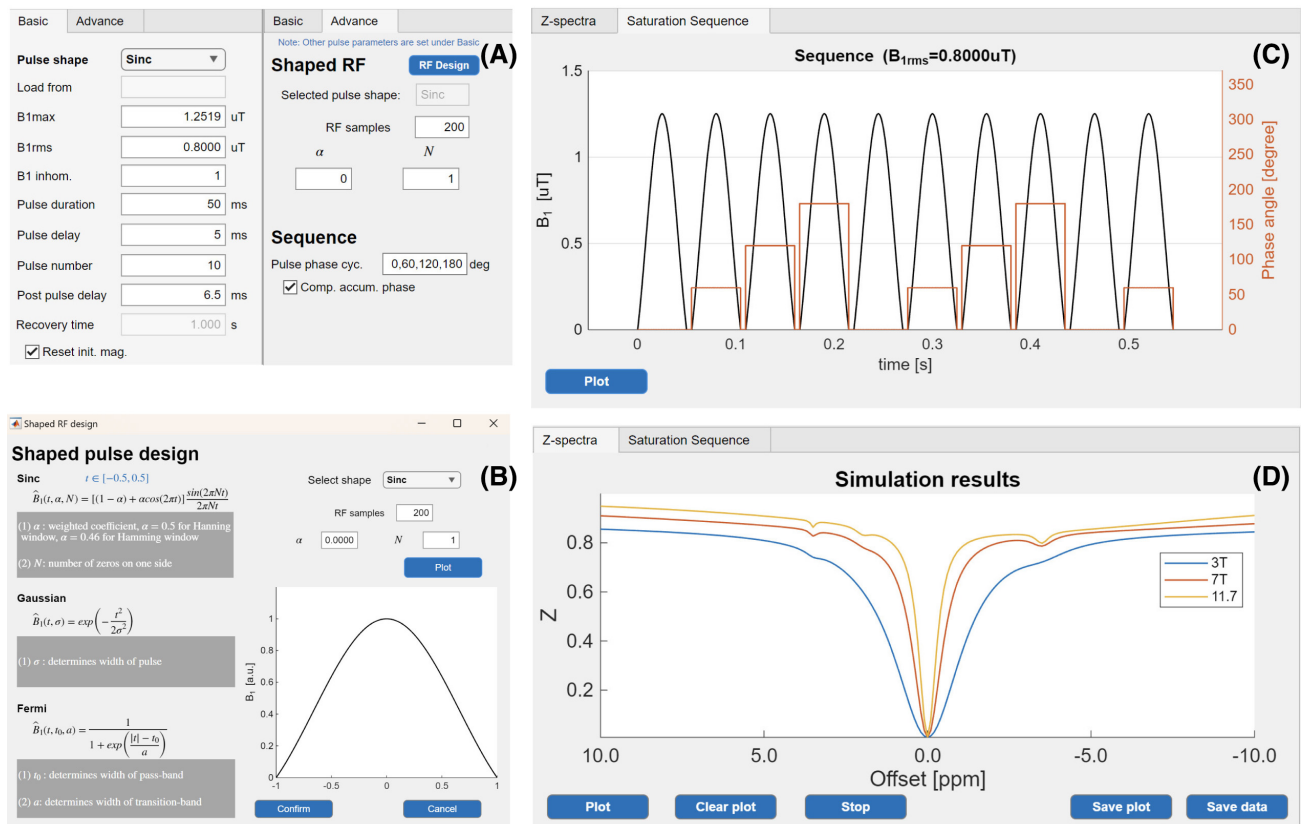


FIGURE 2 Demonstration of the saturation sequence plot and Z-spectra plot. (A) “Basic” and “Advance” tabs to define a pulsed-CEST sequence. (B) “Shaped RF design” window, pops up by clicking the “RF Design” button. (C) Saturation sequence plot of the user-defined sequence, featuring a 50 ms Sinc pulse repeated 10 times, with an interpulse delay of 5 ms, $B_{1\text{rms}} = 0.8 \mu\text{T}$, and a pulse phase cycling pattern of [0, 60, 120, 180] degrees. (D) Z-spectra at 3T, 7T, and 11.7T were simulated using a 2 s, 0.8 μT CW saturation pulse.

2.2.2 | Exchange Settings

In the “Exchange Settings” module, users can define up to eight pools using input boxes. Each pool is characterized by five CEST parameters: the longitudinal relaxation time (T_1), the transverse relaxation time (T_2), the exchange rate from a specific pool to water (k), the frequency offset relative to water (w), and the concentration of exchangeable protons to water protons (f). Pools with zero values for T_1 or T_2 are excluded from the calculations. All chemical exchange parameters can be imported from EXCPARA-files (configuration files used in CESTsimu) or YAML-files (configuration files used in Pulseq-CEST) using regular expressions and can be exported to EXCPARA-files.

The simulated 1D Z-spectra based on the current saturation and exchange settings will be displayed in the “Z-spectra” tab (Figure 2A). Multiple Z-spectra with different simulation settings can be plotted simultaneously using the “Plot” button and saved in MAT-files using the “Save data” button. The legend of each Z-spectrum is customized by user in a pop-up text box. Additionally, the

saturation module can be visualized in the “Saturation Sequence” tab, as shown in Figure 2C.

2.2.3 | Phantom Settings

CESTsimu offers both spectral (1D Z-spectra) and spatial (2D phantom) CEST simulations. In the “Phantom Settings” module, users can customize 2D phantoms with varying shapes, sizes, and numbers, under specific CEST parameter settings and Gaussian noise conditions. The “Shape” drop-down menu provides three options (circle, square, and triangle), while the “Size” slider adjusts the phantom radius. The “Phantom number” field defines the number of phantoms in the field of view (FOV). Exchange parameters for each phantom can be configured in the “Phantom Experiment Setting” window (as shown in Figure 3B) accessed via the “Exp. setting” button. Settings can also be imported from a formatted .MAT file or saved using the “Save data” button. Phantoms are indexed sequentially, starting from the top-left to the bottom-right corner of the 2D image. Enabling the checkbox “Gauss

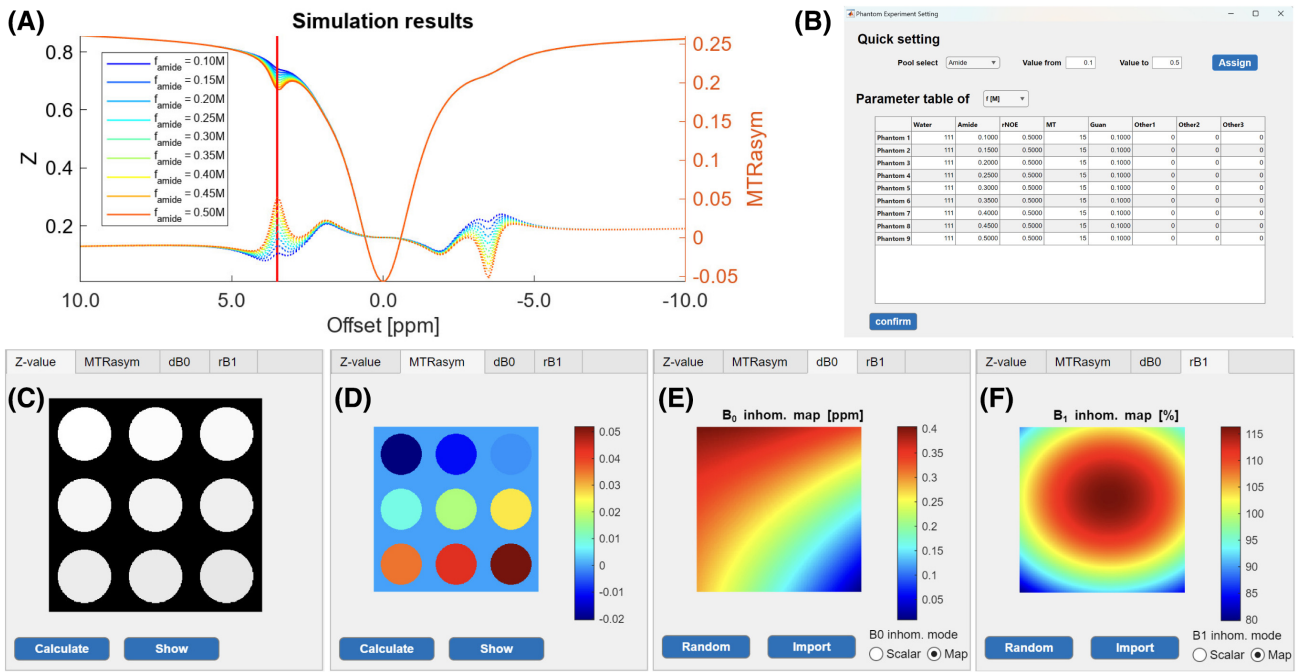


FIGURE 3 Demonstration of the “Phantom Settings” module in CESTsimu. The simulation results are generated with amide concentrations ranging from 0.1 to 0.5 M. (A) 1D average Z-spectra for all nine phantoms. (B) “Phantom Experiment Setting” window (pops up by clicking the “Exp. setting” button in the “Phantom Settings” module) to define exchange parameters for each phantom. (C) Grayscale Z-value images at 3.5 ppm. (D) MTR_{asym} color maps at 3.5 ppm. The red solid line in (A) indicates that the frequency offset for (C) and (D) is 3.5 ppm. (E,F) Randomly generated ΔB_0 map (e) and rB₁ map (F).

noise” adds Gaussian noise, with a user-defined standard deviation “ σ ”, to the simulated Z-spectra using MATLAB’s “randn” function.

Simulated grayscale Z-value images and magnetization transfer ratio asymmetry (MTR_{asym}) color maps are displayed in the lower half of the “Phantom Settings” module. The MTR_{asym} maps are computed using $MTR_{asym}(\Delta\omega) = [S(-\Delta\omega) - S(\Delta\omega)]/S_0$.⁷ The “Freq. offs.” slider selects the frequency offset for the 2D CEST results, while the “Exchange Settings” module automatically updates the 1D Z-spectrum plot with a red cursor marking the selected offset. This displays the corresponding Z-spectra for all phantoms, as shown in Figure 3.

CESTsimu can simulate 2D CEST phantom images under spatially inhomogeneous B₀ and B₁ fields. In the “dB0” and “rB1” tabs of the “Phantom Settings” module, users can set global inhomogeneity values for B₀/B₁ in “Scalar” mode or generate 2D random inhomogeneity maps in “Map” mode. The B₀ inhomogeneity map (ΔB_0 map) is calculated using a simplified second-order spherical harmonic function,^{50,51} excluding terms related to the slice selection coordinate (z):

$$\Delta B_0(x, y) = G_0 + G_x \cdot x + G_y \cdot y + G_{x^2-y^2} \cdot (x^2 - y^2) + G_{xy} \cdot xy, \quad (7)$$

where the zero-order global B₀ inhomogeneity G_0 varies randomly between -1 and 1 ppm, while the first-order coefficients G_x and G_y range from -0.02 to 0.02 ppm/cm, and the second-order coefficients $G_{x^2-y^2}$ and G_{xy} vary from -0.001 to 0.001 ppm/cm². For relative B₁ inhomogeneity map (rB₁ map), CESTsimu uses a Gaussian function with random coefficient a to model the distribution, which is negatively correlated with distance from the magnetic bore center and ranges from 80% to 120% of B_{1max} . Second-order polynomial terms ($C_x, C_y, C_{x^2}, C_{y^2}$) are applied for additional spatial variability, resulting in a random rB₁ map:

$$rB_1(x, y) = B_{1max} \cdot e^{x^2/a^2} \cdot e^{y^2/a^2} \cdot (1 + C_x \cdot x + C_y \cdot y + C_{x^2} \cdot x^2 + C_{y^2} \cdot y^2). \quad (8)$$

2.3 | Experiment

Four experiments were designed to validate the accuracy and practicality of CESTsimu. The simulated data were exported as MAT-files containing variables defined by CESTsimu. Further post-processing and comparison were carried out using custom-written MATLAB code (MathWorks, USA).

2.3.1 | 1D Z-spectrum simulation

To demonstrate the capabilities of 1D Z-spectra simulation in CESTsimu, simulations were conducted with various saturation settings (recovery time T_{rec} , $B_{1\text{max}}$, and saturation time T_{sat}) and exchange settings (fraction and exchange rate of the Guan pool), and the step-by-step process is outlined below:

- Edit the default parameters in the “Saturation Settings”: $B_0 = 3T$, $B_{1\text{max}} = 0.8 \mu\text{T}$, $T_{\text{sat}} = 2 \text{ s}$ (CW), Frequency offsets uniformly spaced from -10 to 10 ppm in 0.05 ppm steps, and M_0 acquired at -300 ppm . Reset the magnetization vector to a steady state for each repetition time (TR) by checking the “Reset init. mag.” checkbox.
- Edit the default five exchange pools in the “Exchange Settings”: water ($T_1/T_2 = 1/0.04 \text{ s}$, $w = 0 \text{ ppm}$, $f = 111 \text{ M}$), amide ($T_1/T_2 = 1/0.1 \text{ s}$, $k = 50 \text{ Hz}$, $w = 3.5 \text{ ppm}$, $f = 0.1 \text{ M}$), NOE ($T_1/T_2 = 1.3/0.005 \text{ s}$, $k = 20 \text{ Hz}$, $w = -3.5 \text{ ppm}$, $f = 0.5 \text{ M}$), MT ($T_1/T_2 = 1/0.00004 \text{ s}$, $k = 30 \text{ Hz}$, $w = -2.5 \text{ ppm}$, $f = 15 \text{ M}$), and Guan ($T_1/T_2 = 1/0.1 \text{ s}$, $k = 400 \text{ Hz}$, $w = 2 \text{ ppm}$, $f = 0.1 \text{ M}$).
- Change a specific saturation or exchange parameter (e.g., the T_{sat} in the “Pulse duration” input box), then click the “Plot” button and type the legend text in the pop-up box.
- Repeat step 3 until all Z-spectra of interest are simultaneously shown in the “Z-spectra” region. Click the “Save data” button to export the simulated data to a .MAT file, in which the “zspecHoldonCell” variable will store all Z-spectra and the corresponding frequency offsets.
- Click the “Clear plot” button to clear all plots in the “Z-spectra” region, and repeat the above steps.

2.3.2 | 2D Phantom experiment

To demonstrate the capabilities of CESTsimu in simulating 2D CEST experiment, data with varying concentrations in multiple phantoms were generated using the following steps:

- Edit the default parameters in the “Saturation Settings”: $B_0 = 3T$, $B_{1\text{max}} = 0.8 \mu\text{T}$, $T_{\text{sat}} = 2 \text{ s}$ (CW), 47 frequency offsets ranging from -10 to 10 ppm in 0.25 ppm steps, and M_0 acquired at -300 ppm . Reset the magnetization vector for each TR.
- Edit the default four exchange pools in the “Exchange Settings”: water ($T_1/T_2 = 1/0.04 \text{ s}$, $w = 0 \text{ ppm}$,

$f = 111 \text{ M}$), amide ($T_1/T_2 = 1/0.1 \text{ s}$, $k = 50 \text{ Hz}$, $w = 3.5 \text{ ppm}$, $f = 0.1 \text{ M}$), NOE ($T_1/T_2 = 1.3/0.005 \text{ s}$, $k = 20 \text{ Hz}$, $w = -3.5 \text{ ppm}$, $f = 0.5 \text{ M}$), and MT ($T_1/T_2 = 1/0.00004 \text{ s}$, $k = 30 \text{ Hz}$, $w = -2.5 \text{ ppm}$, $f = 15 \text{ M}$).

- Configure the experiment settings by clicking the “Exp. setting” button. Edit the exchange parameters of interest for each phantom in the “Phantom Experiment Settings” window as shown in Figure 3B. The experiment parameters can either be edited individually or assigned linear-varying values by clicking the “Assign” button. The indexing of the phantoms follows a sequential order, starting from the upper-left to the bottom-right.
- Click the “Calculate” button. Upon completion, both the Z-value map and MTR_{asym} map will be displayed in the “Phantom Settings” module. Simultaneously, the averaged Z-spectra of each phantom at the corresponding frequency offset will be plotted in the “Exchange Settings” module.
- Click the “Save data” button to export the Z-value map and MTR_{asym} map as the “img” and “img_MTR” variables in a .MAT file for further processing.

The simulated 2D CEST phantom experiment was first demonstrated with different phantom numbers of 5, 9, and 13. Gaussian noise ($\sigma = 0, 0.0016$, and 0.0064) was added to the simulated Z-spectra of nine phantoms, and the exported data was analyzed using the multi-pool Lorentzian fitting (MPLF) method¹⁷ to validate the settings and noise addition. Here, the MPLF considered four pools including direct water saturation (DS), amide, NOE, and MT.

2.3.3 | 2D B_0 and B_1 inhomogeneity experiment

To demonstrate CESTsimu’s simulation of B_0 and B_1 inhomogeneity, 2D CEST phantom data was generated:

- Edit the saturation parameters in the “Saturation Settings”: $B_0 = 3T$, $3.7 \mu\text{T}$ CW with a 5 ms duration, frequency offsets ranging from -2 to 2 ppm in 0.05 ppm steps, and M_0 acquired at -300 ppm . The magnetization vector was reset for each TR. The exchange pools in the “Exchange Settings” module was set to match those in Experiment 2.3.1.
- Configure phantom experiment parameters in the “Phantom Experiment Settings” window by clicking the “Exp. setting” button. The T_1 values of water were varied from 0.6 to 3.8 s in increments of 0.4 s for nine phantoms, mimicking the contrasts between brain tissues and cerebrospinal fluid (CSF).⁵²

- Generate random ΔB_0 and rB_1 maps by clicking the “Random” button in the “dB0” and “rB1” tabs respectively, as shown in Figure 3E,F.
- Switch to the “Z-value” tab and click the “Calculate” button. After the calculation is completed, click the “Save data” button to export the simulated data.

The simultaneous mapping of water shift and B_1 (WASABI) method⁵³ was further applied to analyze the CESTsimu data, using the following WASABI model:

$$Z(\Delta\omega) = \left| c - d \cdot \sin^2 \left(\tan^{-1} \left(\frac{\gamma \cdot B_1}{\Delta\omega - \delta\omega} \right) \right) \cdot \sin^2 \left(\sqrt{(\gamma \cdot B_1)^2 + (\Delta\omega - \delta\omega)^2} \cdot \frac{t_p}{2} \right) \right|, \quad (9)$$

where $|\cdot|$ denotes the absolute value operator, with c and d accounting for relaxation effects, B_1 representing the RF amplitude, and $\delta\omega$ being the water frequency shift. Other parameters include the saturation pulse duration t_p and the frequency offset $\Delta\omega$.

The WASABI lookup table was created using Equation (9) with rB_1 ranging from 0.8 to 1.2 in 0.01 steps, $\delta\omega$ from -0.5 to 0.5 ppm in 0.01 steps, c from 0.2 to 1 in 0.1 steps, and d from 0.5 to 2 in 0.1 steps. The four parameters for each voxel were determined by a minimum-search approach.

2.3.4 | BMsim challenge validation

We tested CESTsimu’s robustness by simulating the Z-spectra of eight BMsim challenge cases (https://github.com/pulseq-cest/BMsim_challenge)³⁷ and comparing the results with Pulseq-CEST (<https://pulseq-cest.github.io/>)⁴¹ with the primary settings detailed in Table 1.

TABLE 1 Main simulation settings for the eight cases provided by the BMsim challenge.

Case	Pulse shape	T_{sat}	Pool	Pulse number
1	CW (2 μT)	15 s	2 pools	1
2	CW (2 μT)	2 s	2 pools	1
3	CW (2 μT)	2 s	5 pools	1
4	CW (3.7 μT)	5 ms	5 pools	1
5	Gaussian (1.9962 μT , 50 ms)	50 ms	2 pools	1
6	Gaussian (1.9962 μT , 50 ms)	1.975 s	2 pools	36
7	Gaussian (1.9962 μT , 50 ms)	1.975 s	5 pools	36
8	CW (3.7 μT , 5 ms)	10.1 ms	5 pools	2

Note: The amplitude of the CW is represented as the maximum B_1 value, while the amplitude of the Gaussian pulse is shown as the root-mean-square B_1 value.

3 | RESULTS

3.1 | 1D Z-spectrum simulation

Results in Figure 4A–C display the simulated Z-spectra under various saturation settings. Figure 4A shows that increasing T_{rec} elevates the Z-spectrum to larger values (e.g., from 0.8288 to 0.8444 at 8 ppm), indicating more signal recovery from a prolonged relaxation period. Results in Figure 4B illustrate that an increase in B_1 causes DS/MT confounding effects to become more prominent, obviously masking other CEST effects. Results in Figure 4C demonstrate that extending the T_{sat} leads to an increase in CEST/DS/MT effects until reaching a steady state. These results exhibit the capability of CESTsimu in simulating 1D Z-spectra under different saturation (B_0 and B_1) settings.

Simulation results with varying exchange settings are displayed in Figure 4D–G. Here, we utilized the Guan CEST for the demonstration. Results in Figure 4D,E show that an increase in Guan concentration from 0 to 100 mM results in an increase in the +2.0 ppm MTR_{asym} signal from -0.0087 to 0.0163. The negative MTR_{asym} value of Guan CEST was caused by the presence of the NOE and MT effects. Results in Figure 4F–G demonstrate that an increase in Guan exchange rate from 200 to 1000 Hz correlates with an increase in MTR_{asym} values from 0.0032 to 0.0213. These observations exhibit the capability of CESTsimu in simulating 1D Z-spectra under different exchange (concentration and exchange rate) settings.

3.2 | 2D CEST phantom experiment

In the 2D CEST phantom experiment, we utilized CESTsimu to generate the 2D CEST phantoms with varied

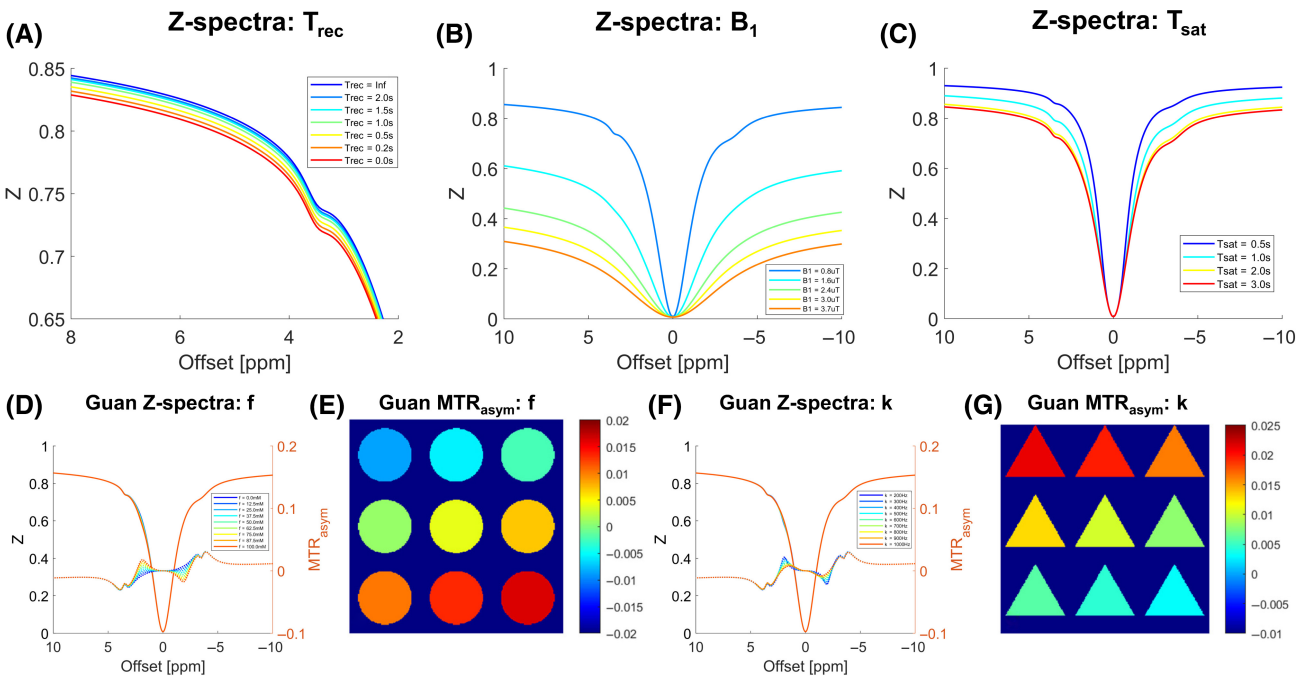


FIGURE 4 Simulation results from CESTsimu with various settings are presented as follows: (A) Z-spectra with T_{rec} values of 0, 0.2, 0.5, 1.0, 1.5, 2.0 s, and infinity (which is realized by checking the “Reset init. mag.” checkbox). (B) Z-spectra with B_1 values of 0.8 μ T, 1.6 μ T, 2.4 μ T, and 3.0 μ T. (C) Z-spectra with T_{sat} of 0.5, 1.0, 2.0, and 3.0 s. (D,E) ROI-averaged Z-spectra and MTR_{asym} maps (at 2 ppm) with Guan concentrations ranging from 0 to 100 mM in 12.5 mM increments. (F,G) ROI-averaged Z-spectra and MTR_{asym} maps (at 3.5 ppm) with Guan exchange rates ranging from 200 to 1000 Hz in 100 Hz increments.

amide concentrations. Simulated Z-value images and calculated MTR_{asym} images at 3.5 ppm are shown in Figure 5. As we can see, users can easily define the number of phantoms (5, 9, and 13 are presented here) by changing the “Phantom number” under the “Phantom Settings” module. An obvious gradient trend in image intensity is observed in both Z-value images and MTR_{asym} images, reflecting the linear changes in amide concentration. With amide concentration ranging from 0 to 40 mM, the intensity of MTR_{asym} images spans from negative to positive values. The presence of negative values in MTR_{asym} at 3.5 ppm is attributed to the influence of NOE and MT effects, which partially offsets the amide signal.

The MPLF-calculated amide amplitude maps and their correlations with amide concentration defined in CESTsimu are shown in Figure 6. The sum of squares due to error (SSE) and goodness of fit (R^2) for the three noise levels ($\sigma = 0$, 0.0016, and 0.0064) are [0.0128, 0.9995], [0.1006, 0.9963], and [1.0838, 0.9571], respectively. Nine phantoms with a gradient change in amide concentration are well distinguishable under three noise levels, as shown in Figure 6A–C. Despite the noise level of $\sigma = 0.0064$ causing large variation in the amide amplitude map in Figure 6C, MPLF can still robustly extract the concentration-dependent amplitude ($R^2 = 0.9571$).

3.3 | 2D B_0 and B_1 inhomogeneity experiment

The comparison results of the ΔB_0 and rB_1 maps obtained by WASABI and its corresponding ground truth generated by CESTsimu are shown in Figure 7. Generally, the ΔB_0 and rB_1 maps calculated by WASABI is comparable to the ground truth provided by CESTsimu. The standard deviation (SD) was 0.0106 for the calculated ΔB_0 map and 0.0066 for the rB_1 map, respectively. The Bland-Altman plot reveals periodic errors, highlighting the limitations in the accuracy of the simple minimum-search approach that relies on predefined lookup tables. These periodic errors could be further reduced by subsequent WASABI model fitting recommended in the original WASABI paper.⁵³

3.4 | BMsim challenge validation

The simulation results for Cases 1–4 are presented in Figure 8, where the Z-spectra simulated by CESTsimu closely match those obtained from Pulseq-CEST, with maximum discrepancies of less than 0.00075. These cases employ a CW for saturation, resulting in relatively low simulation complexity.

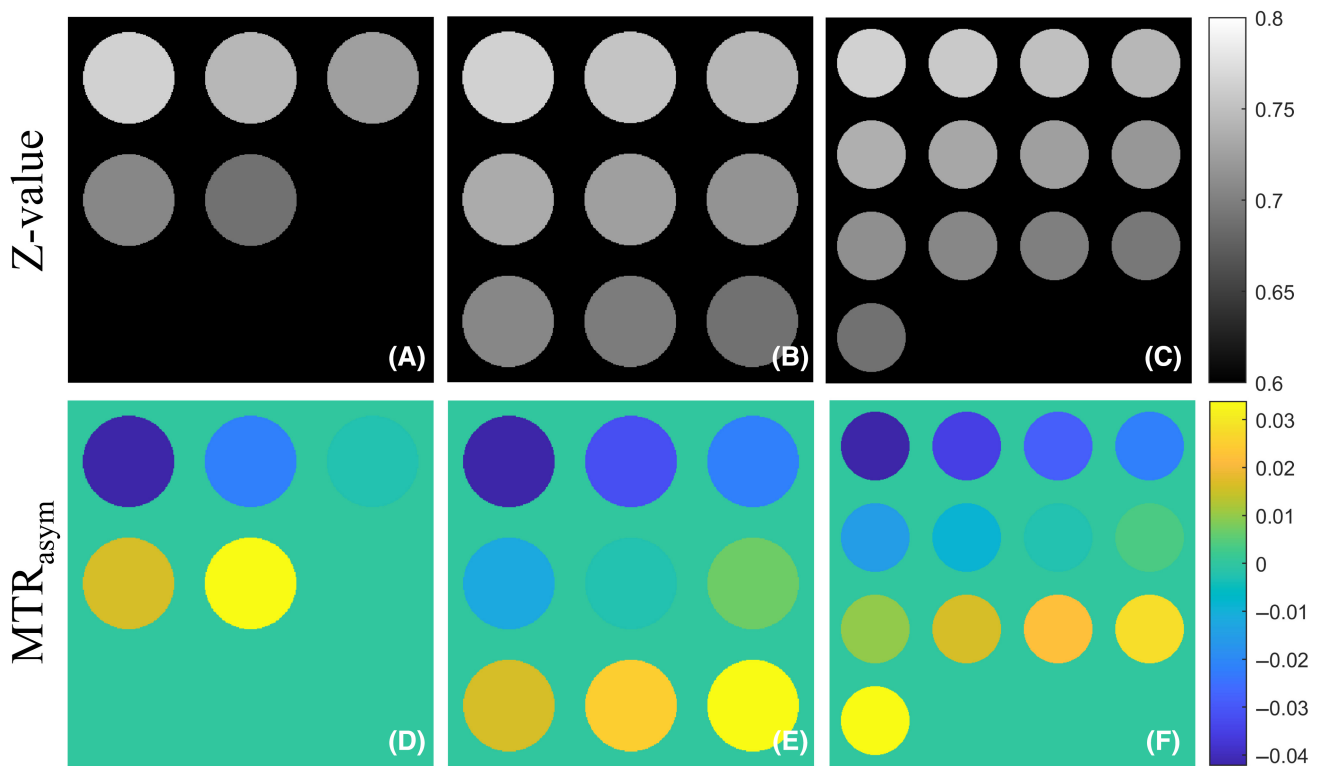


FIGURE 5 Z-value (A–C) and MTR_{asym} (D,E) images at 3.5 ppm with different phantom numbers.

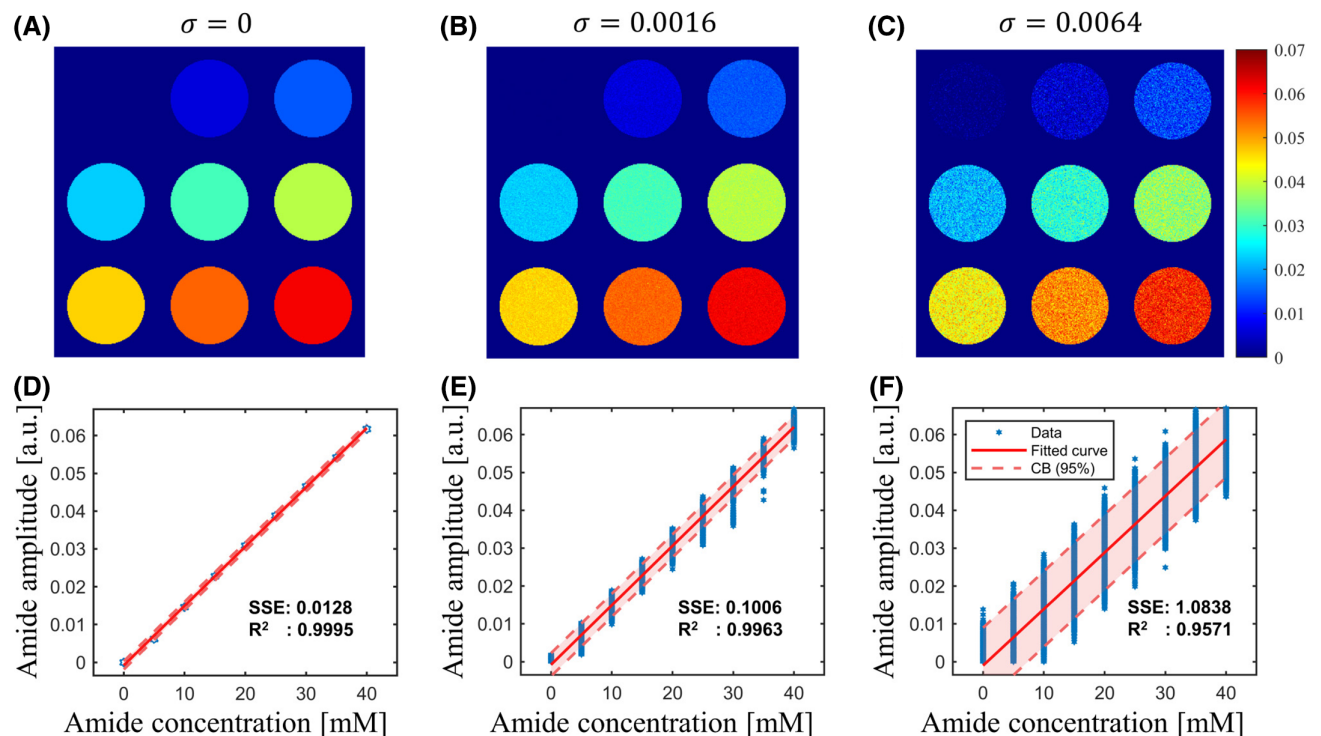


FIGURE 6 CEST simulation results under different Gaussian noise levels analyzed using MPLF. (A–C) Amide amplitude maps obtained by MPLF with standard deviations σ of 0, 0.0016, and 0.0064. (D–F) Corresponding linear regression results with 95% simultaneous confidence bands (CB).

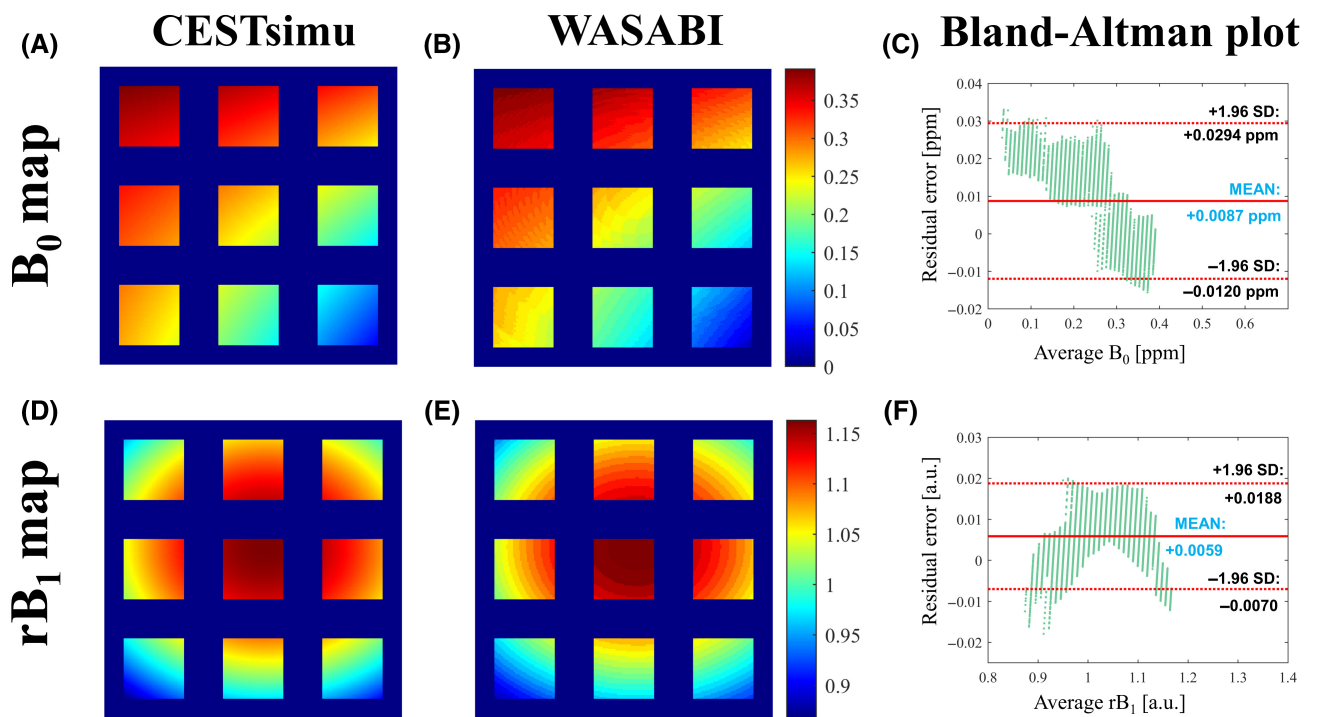


FIGURE 7 ΔB_0 and rB_1 maps simulated by CESTsimu (A,D) and measured using WASABI (B,E), along with the Bland-Altman plot comparing B_0 and B_1 values from CESTsimu and WASABI (C,F).

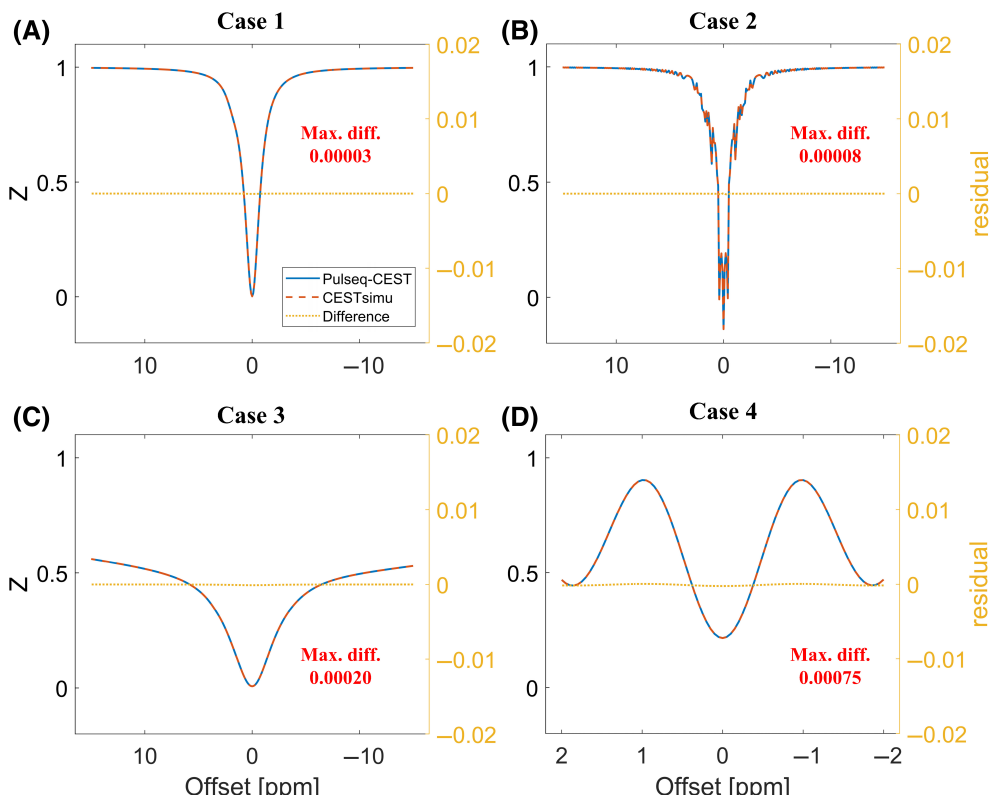


FIGURE 8 Simulation results on BMsim challenge Cases 1–4 obtained by CESTsimu and Pulseq-CEST. (A) Amide proton transfer (APT) steady-state preparation. (B,C) APT transient-state preparation. (D) WASABI preparation.

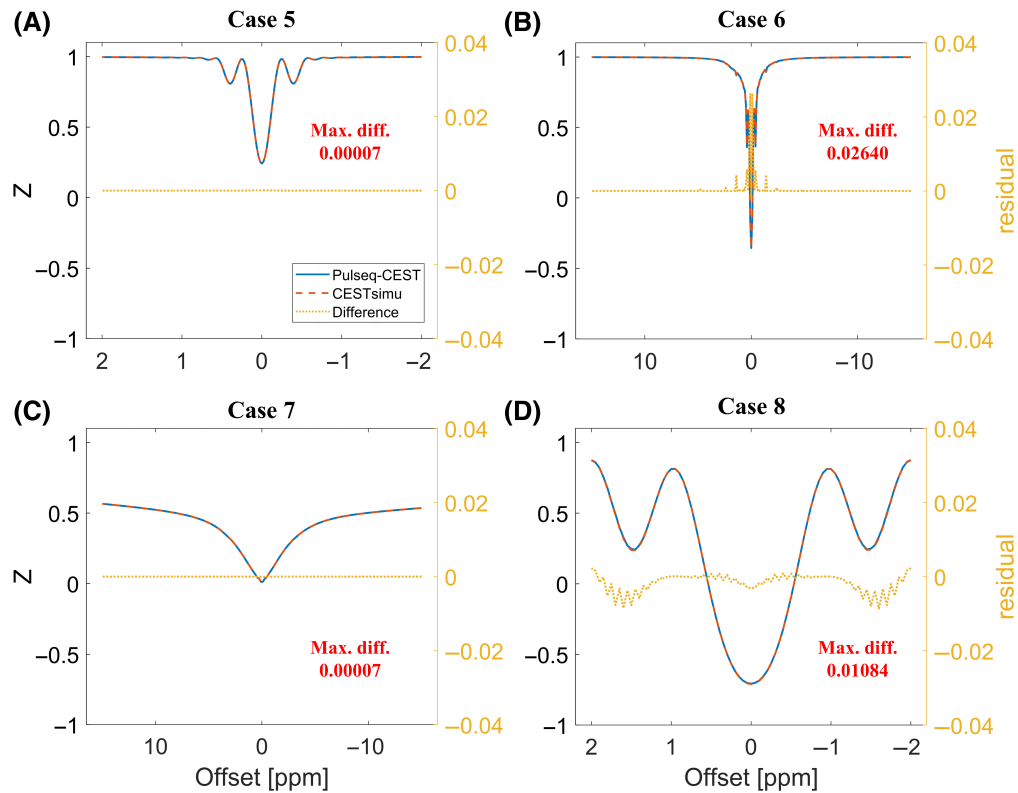


FIGURE 9 Simulation results on BMsim challenge Cases 5–8 obtained by CESTsimu and Pulseq-CEST. (A) Single-shaped pulse APT preparation. (B,C) Pulsed APT preparation. (D) WASABI preparation.

The simulation results for Cases 5–8 are displayed in Figure 9. The Z-spectra simulated by CESTsimu in Cases 5 and 7 closely match those obtained from Pulseq-CEST, with maximum discrepancies of less than 0.00007. However, observable differences are found in Cases 6 and 8, where pulsed saturation is introduced and the complexity of the Z-spectra is increased. In Case 6, the water pool and the Guan pool (at 1.9 ppm, $k = 50$ Hz) are in close proximity, making the Z-spectra highly sensitive to simulation accuracy. A maximum deviation of 0.0264 is observed around water at ± 0.1 ppm of the Z-spectra (Figure 9B), with additional significant differences at ± 0.4 and ± 1.4 ppm. In Case 8, there are pronounced differences in the lateral regions outside, with a maximum discrepancy of 0.01084 at around ± 1.6 ppm.

4 | DISCUSSION

In this study, we developed a user-friendly CEST simulation tool (CESTsimu) with a GUI using MATLAB App for intuitively simulating 1D Z-spectra or 2D CEST phantom data. Results of four experiments, including 1D Z-spectrum simulation, 2D CEST phantom experiment, 2D B_0 and B_1 inhomogeneity experiment and BMsim challenge validation, demonstrated that CESTsimu could accurately and robustly generate the 1D Z-spectra and 2D CEST phantom data. Moreover, CESTsimu with a GUI provides

users with large flexibility to customize the parameters based on their experimental design.

The 1D and 2D experimental results demonstrate the accuracy and practicality of CESTsimu. For accuracy, the high correlation between the CEST signals and defined concentrations in the 2D experiments confirms that the simulation results align well with theoretical ground truth (Figure 6). Additionally, the observed influences of saturation parameters on Z-spectra (Figure 4) are similar to previously reported theoretical trends,⁴⁹ validating the reliability of CESTsimu. In terms of practicality, the software enables users to effortlessly customize saturation and exchange parameters for CEST simulation. The user-friendly interface simplifies the entire simulation process, eliminating the need for code modifications. Furthermore, the software offers comprehensive features, including 2D CEST simulation with various shapes and quantities of phantoms, and the optional incorporation of the influence of 1D/2D B_0 and B_1 inhomogeneity. Preliminary sequence protocol optimization on parameters like T_{rec} and T_{sat} ⁵⁴ can be performed on CESTsimu, highlighting its exceptional utility and versatility.

Guan CEST imaging is challenging at 3T because of its fast exchange rate in solution and the confounding effect from neighboring amide signal.⁵⁴ This issue is corroborated by the simulation results presented in Figure 4F, which demonstrate that the 100 mM Guan signal becomes nearly undetectable when the exchange rate surpasses

600 Hz. A recent study by Zhang et al.⁵⁵ has reported relatively low exchange rates of Guan CEST in the mouse brain (240–480 Hz), demonstrating the theoretical feasibility of Guan CEST imaging at 3T. Given that both the saturation module and post-processing methods require meticulous optimization for detecting the subtle Guan signal, CESTsimu offers a valuable tool for users to conduct such offline sequence optimization and post-experiment validation.

Although CESTsimu shows a notable discrepancy with Pulseq-CEST in Cases 6 and 8 (Figure 9), it is important to acknowledge that there is currently no definitive ground truth for CEST simulation.³⁷ The absence of standardized simulation protocols within the CEST community poses a significant challenge, as simulation outcomes can be affected by various factors, including the mathematical principals of BME solvers,⁵⁶ numerical precision, and code settings such as variable initializations during iterations. Establishing common CEST simulation standards is essential for advancing techniques like quantitative CEST and requires collective efforts from the community. We are committed to integrating future insights from the BMsim challenge to enhance the accuracy and adaptability of the CESTsimu framework.

Currently, CESTsimu has two main limitations. First, it cannot simulate sequences where different TRs have varying pulse shapes or interpulse delays, nor does it allow users to define the MT lineshape,⁵⁷ such as a super-Lorentzian model.⁵⁸ Second, computation time becomes a significant issue when accounting for B_0 and B_1 spatial inhomogeneity, especially when Z-spectra must be calculated for each voxel. While generating a single Z-spectrum is extremely fast, CESTsimu requires approximately 70 min to compute 2D CEST data for over 54 000 voxels. Future development could focus on integrating the option to select different BME solvers or including parallel computation, thereby improving its versatility and adaptability to various simulation requirements.

Nevertheless, CESTsimu provides a user-friendly GUI that can simulate CEST experiments in both 1D and 2D modes, demonstrating significant promise in fulfilling various needs and appealing to a wide range of users. First, as a pedagogical tool, it provides an intuitive platform for understanding how experimental parameters like saturation settings, B_0/B_1 inhomogeneities, and exchange parameters affect the Z-spectrum. This can help new CEST researchers gain insights into the mechanisms of CEST contrast. Second, CESTsimu offers a reliable phantom simulation framework to improve the interpretation of *in vivo* CEST measurements. While previous studies²² have used BME simulation to investigate the impact of T_2 variation on measured CEST signals, CESTsimu provides a

more comprehensive phantom experiment setup to visualize the joint impacts of parameters like exchange rate and B_0/B_1 inhomogeneities. Third, the MPLF experiment (Figure 6) and WASABI experiment (Figure 7) demonstrate that data generated by CESTsimu can be readily used to evaluate various CEST analysis methods. It is expected that CESTsimu can also be used to generate CEST data for supporting the quantitative CEST experiments (e.g., QUEST/QUEST,³⁴ QUASS,⁵⁹ MR fingerprinting,⁶⁰ etc.). Since the saturation setting and the exchange setting are available as ground truth, the accuracy and robustness of these CEST quantification methods can be evaluated.

5 | CONCLUSIONS

We have developed a user-friendly CESTsimu GUI that allows for intuitive CEST simulation in both spectral (1D Z-spectra) and spatial (2D CEST phantom) modes. With CESTsimu, users can easily conduct CEST simulation experiments with varied saturation and exchange settings. Additionally, CESTsimu GUI is compatible with other CEST simulation platform (Pulseq-CEST). CESTsimu is capable of mimicking offline CEST experiments under customized experimental designs, making it accessible to a wide range of users and facilitating a broad utilization of CEST MRI.

ACKNOWLEDGEMENTS

We gratefully acknowledge the funding support from the National Natural Science Foundation of China (82402225), Li Ka Shing Faculty of Medicine, The University of Hong Kong (109000487, 204610401, 204610519, 200000341, and 109001694) and the Health and Medical Research Fund (21222621). We also thank Dr. Moritz Zaiss, Dr. Patrick Schuenke, and Dr. Kai Herz for their open-source CEST simulation tools, which were utilized for comparisons in this study. Additionally, we appreciate the ISMRM Reproducible Research Study Group for conducting a code review of the code (CESTsimu Version 0.7) supplied in the Data Availability Statement. The scope of the code review covered only the code's ease of download, quality of documentation, and ability to run, but did not consider scientific accuracy or code efficiency.

DATA AVAILABILITY STATEMENT

The CESTsimu GUI and its source code are publicly available at: <https://github.com/JianpanHuang/CESTsimu>.

ORCID

Huabin Zhang  <https://orcid.org/0000-0002-5170-2753>
Bensheng Qiu  <https://orcid.org/0000-0003-2987-7378>

Jiadi Xu  <https://orcid.org/0000-0001-9698-5622>
Kannie WY Chan  <https://orcid.org/0000-0002-7315-1550>
Jianpan Huang  <https://orcid.org/0000-0002-4453-8764>

REFERENCES

1. Zhou J, Payen J-F, Wilson DA, Traystman RJ, Van Zijl PC. Using the amide proton signals of intracellular proteins and peptides to detect pH effects in MRI. *Nat Med.* 2003;9:1085-1090.
2. Van Zijl PC, Yadav NN. Chemical exchange saturation transfer (CEST): what is in a name and what isn't? *Magn Reson Med.* 2011;65:927-948.
3. Heo HY, Tee YK, Harston G, Leigh R, Chappell MA. Amide proton transfer imaging in stroke. *NMR Biomed.* 2023;36:e4734.
4. Cai K, Haris M, Singh A, et al. Magnetic resonance imaging of glutamate. *Nat Med.* 2012;18:302-306.
5. Kogan F, Singh A, Debrosse C, et al. Imaging of glutamate in the spinal cord using GluCEST. *Neuroimage.* 2013;77:262-267.
6. Davis KA, Nanga RPR, Das S, et al. Glutamate imaging (GluCEST) lateralizes epileptic foci in nonlesional temporal lobe epilepsy. *Sci Transl Med.* 2015;7:309ra161.
7. Zhou J, Hong X, Zhao X, Gao JH, Yuan J. APT-weighted and NOE-weighted image contrasts in glioma with different RF saturation powers based on magnetization transfer ratio asymmetry analyses. *Magn Reson Med.* 2013;70:320-327.
8. Jones CK, Huang A, Xu J, et al. Nuclear Overhauser enhancement (NOE) imaging in the human brain at 7 T. *Neuroimage.* 2013;77:114-124.
9. Huang J, Han X, Chen L, Xu X, Xu J, Chan KW. Relayed nuclear Overhauser enhancement imaging with magnetization transfer contrast suppression at 3 T. *Magn Reson Med.* 2021;85:254-267.
10. Chan KW, McMahon MT, Kato Y, et al. Natural D-glucose as a biodegradable MRI contrast agent for detecting cancer. *Magn Reson Med.* 2012;68:1764-1773.
11. Walker-Samuel S, Ramasawmy R, Torrealdea F, et al. In vivo imaging of glucose uptake and metabolism in tumors. *Nat Med.* 2013;19:1067-1072.
12. Knutsson L, Xu X, Zijl PC, Chan KW. Imaging of sugar-based contrast agents using their hydroxyl proton exchange properties. *NMR Biomed.* 2023;36:e4784.
13. Haris M, Nanga RPR, Singh A, et al. Exchange rates of creatine kinase metabolites: feasibility of imaging creatine by chemical exchange saturation transfer MRI. *NMR Biomed.* 2012;25:1305-1309.
14. Chen L, Barker PB, Weiss RG, Zijl PC, Xu J. Creatine and phosphocreatine mapping of mouse skeletal muscle by a polynomial and Lorentzian line-shape fitting CEST method. *Magn Reson Med.* 2019;81:69-78.
15. Xu J, Chung JJ, Jin T. Chemical exchange saturation transfer imaging of creatine, phosphocreatine, and protein arginine residue in tissues. *NMR Biomed.* 2023;36:e4671.
16. Wang K, Huang J, Ju L, et al. Creatine mapping of the brain at 3T by CEST MRI. *Magn Reson Med.* 2024;91:51-60.
17. Zaiss M, Schmitt B, Bachert P. Quantitative separation of CEST effect from magnetization transfer and spillover effects by Lorentzian-line-fit analysis of z-spectra. *J Magn Reson.* 2011;211:149-155.
18. Huang J, Lai JH, Tse KH, et al. Deep neural network based CEST and AREX processing: application in imaging a model of Alzheimer's disease at 3 T. *Magn Reson Med.* 2022;87:1529-1545.
19. Zhou J, Lal B, Wilson DA, Laterra J, Van Zijl PC. Amide proton transfer (APT) contrast for imaging of brain tumors. *Magn Reson Med.* 2003;50:1120-1126.
20. Zaiss M, Windschuh J, Paech D, et al. Relaxation-compensated CEST-MRI of the human brain at 7 T: unbiased insight into NOE and amide signal changes in human glioblastoma. *Neuroimage.* 2015;112:180-188.
21. Haris M, Nath K, Cai K, et al. Imaging of glutamate neurotransmitter alterations in Alzheimer's disease. *NMR Biomed.* 2013;26:386-391.
22. Huang J, Xu J, Lai JH, et al. Relayed nuclear Overhauser effect weighted (rNOEw) imaging identifies multiple sclerosis. *NeuroImage: Clinical.* 2021;32:102867.
23. Liu Z, Wen J, Wang M, et al. Breast amide proton transfer imaging at 3 T: diagnostic performance and association with pathologic characteristics. *J Magn Reson Imaging.* 2023;57:824-833.
24. Crescenzi R, Donahue PM, Mahany H, Lants SK, Donahue MJ. CEST MRI quantification procedures for breast cancer treatment-related lymphedema therapy evaluation. *Magn Reson Med.* 2020;83:1760-1773.
25. Vinogradov E, Keupp J, Dimitrov IE, Seiler S, Pedrosa I. CEST-MRI for body oncologic imaging: are we there yet? *NMR Biomed.* 2023;36:e4906.
26. Deng M, Chen S-Z, Yuan J, Chan Q, Zhou J, Wang YXJ. Chemical exchange saturation transfer (CEST) MR technique for liver imaging at 3.0 Tesla: an evaluation of different offset number and an after-meal and over-night-fast comparison. *Mol Imaging Biol.* 2016;18:274-282.
27. Bloch F. Nuclear induction. *Phys Rev.* 1946;70:460.
28. McConnell HM. Reaction rates by nuclear magnetic resonance. *J Chem Phys.* 1958;28:430-431.
29. Jin T, Chung JJ. Adjustment of rotation and saturation effects (AROSE) for CEST imaging. *Magn Reson Med.* 2024;91:1016-1029.
30. Zhao Y, Sun C, Zu Z. Isolation of amide proton transfer effect and relayed nuclear Overhauser enhancement effect at -3.5 ppm using CEST with double saturation powers. *Magn Reson Med.* 2023;90:1025-1040.
31. Perlman O, Ito H, Herz K, et al. Quantitative imaging of apoptosis following oncolytic virotherapy by magnetic resonance fingerprinting aided by deep learning. *Nat Biomed Eng.* 2022;6:648-657.
32. Chen L, Schär M, Chan KW, et al. In vivo imaging of phosphocreatine with artificial neural networks. *Nat Commun.* 2020;11:1072.
33. Chen L, Xu H, Gong T, et al. Accelerating multipool CEST MRI of Parkinson's disease using deep learning-based Z-spectral compressed sensing. *Magn Reson Med.* 2024;92:2616-2630.
34. McMahon MT, Gilad AA, Zhou J, Sun PZ, Bulte JW, Van Zijl PC. Quantifying exchange rates in chemical exchange saturation transfer agents using the saturation time and saturation power dependencies of the magnetization transfer effect on the magnetic resonance imaging signal (QUEST and QUESP): pH calibration for poly-L-lysine and a starburst dendrimer. *Magn Reson Med.* 2006;55:836-847.

35. Desmond KL, Stanisz GJ. Understanding quantitative pulsed CEST in the presence of MT. *Magn Reson Med.* 2012;67:979-990.
36. Perlman O, Farrar CT, Heo HY. MR fingerprinting for semisolid magnetization transfer and chemical exchange saturation transfer quantification. *NMR Biomed.* 2023;36:e4710.
37. Schuenke P, Herz K, Zu Z, et al. *Validate your CEST simulation!*. ISMRM; 2023.
38. Overall W, Pauly J. *An extensible, graphical environment for pulse sequence design and simulation*. ISMRM; 2007.
39. Stöcker T, Vahedipour K, Pflugfelder D, Shah NJ. High-performance computing MRI simulations. *Magn Reson Med.* 2010;64:186-193.
40. Liu F, Velikina JV, Block WF, Kijowski R, Samsonov AA. Fast realistic MRI simulations based on generalized multi-pool exchange tissue model. *IEEE Trans Med Imaging.* 2016;36:527-537.
41. Herz K, Mueller S, Perlman O, et al. Pulseq-CEST: towards multi-site multi-vendor compatibility and reproducibility of CEST experiments using an open-source sequence standard. *Magn Reson Med.* 2021;86:1845-1858.
42. Layton KJ, Kroboth S, Jia F, et al. Pulseq: a rapid and hardware-independent pulse sequence prototyping framework. *Magn Reson Med.* 2017;77:1544-1552.
43. Trott O, Palmer AG III. $R_1\rho$ relaxation outside of the fast-exchange limit. *J Magn Reson.* 2002;154:157-160.
44. Palmer AG III, Kroenke CD, Loria JP. Nuclear magnetic resonance methods for quantifying microsecond-to-millisecond motions in biological macromolecules. *Methods Enzymol.* 2001;339:204-238.
45. Zaiss M, Bachert P. Chemical exchange saturation transfer (CEST) and MR Z-spectroscopy in vivo: a review of theoretical approaches and methods. *Phys Med Biol.* 2013;58:R221.
46. Zhou J, Zijl PC. Chemical exchange saturation transfer imaging and spectroscopy. *Prog Nucl Magn Reson Spectrosc.* 2006;48:109-136.
47. Shaghaghi M, Cai K. Analytical solution of the Bloch-McConnell equations for steady-state CEST Z-spectra. *Magn Reson Imaging.* 2024;109:74-82.
48. Zhou J, Zaiss M, Knutsson L, et al. Review and consensus recommendations on clinical APT-weighted imaging approaches at 3T: application to brain tumors. *Magn Reson Med.* 2022;88:546-574.
49. Bie C, Zijl P, Xu J, Song X, Yadav NN. Radiofrequency labeling strategies in chemical exchange saturation transfer MRI. *NMR Biomed.* 2023;36:e4944.
50. Juchem C, Graaf RA. B0 magnetic field homogeneity and shimming for in vivo magnetic resonance spectroscopy. *Anal Biochem.* 2017;529:17-29.
51. Gruetter R. Automatic, localized in vivo adjustment of all first-and second-order shim coils. *Magn Reson Med.* 1993;29:804-811.
52. Lu H, Nagae-Poetscher LM, Golay X, Lin D, Pomper M, Van Zijl PC. Routine clinical brain MRI sequences for use at 3.0 Tesla. *J Magn Reson Imaging.* 2005;22:13-22.
53. Schuenke P, Windschuh J, Roeloffs V, Ladd ME, Bachert P, Zaiss M. Simultaneous mapping of water shift and B1 (WASABI)—application to field-inhomogeneity correction of CEST MRI data. *Magn Reson Med.* 2017;77:571-580.
54. Wang K, Ju L, Song Y, et al. Whole-cerebrum guanidino and amide CEST mapping at 3 T by a 3D stack-of-spirals gradient echo acquisition. *Magn Reson Med.* 2024;92:1456-1470.
55. Zhang Z, Wang K, Park S, et al. The exchange rate of creatine CEST in mouse brain. *Magn Reson Med.* 2023;90:373-384.
56. Graf C, Rund A, Aigner CS, Stollberger R. Accuracy and performance analysis for Bloch and Bloch-McConnell simulation methods. *J Magn Reson.* 2021;329:107011.
57. Zaiss M, Jin T, Kim SG, Gochberg DF. Theory of chemical exchange saturation transfer MRI in the context of different magnetic fields. *NMR Biomed.* 2022;35:e4789.
58. Morrison C, Stanisz G, Henkelman RM. Modeling magnetization transfer for biological-like systems using a semi-solid pool with a super-Lorentzian lineshape and dipolar reservoir. *J Magn Reson, Series B.* 1995;108:103-113.
59. Sun PZ. Quasi-steady-state CEST (QUASS CEST) solution improves the accuracy of CEST quantification: QUASS CEST MRI-based omega plot analysis. *Magn Reson Med.* 2021;86:765-776.
60. Perlman O, Herz K, Zaiss M, Cohen O, Rosen MS, Farrar CT. CEST MR-fingerprinting: practical considerations and insights for acquisition schedule design and improved reconstruction. *Magn Reson Med.* 2020;83:462-478.

How to cite this article: Zhang H, Qiu B, Xu J, Chan KW, Huang J. CESTsimu: An open-source GUI for spectral and spatial CEST simulation. *Magn Reson Med.* 2025;1-15. doi: 10.1002/mrm.30430